

Investigation of Crevice Corrosion of AISI 316 Stainless Steel and Ni-Cr-Mo Alloy 625 Using Coupled Multi-Electrode Arrays

Florent Bocher, Noah D. Budiansky and John R. Scully

Materials Science & Engineering

University of Virginia, 116 Engineer's Way

PO Box 400745, Charlottesville, VA 22904-4745

Francisco Presuel-Moreno

Department of Ocean Engineering

Florida Atlantic University, 101 North Beach Road, ST01-239

Dania Beach, Florida, 33004-3023

ABSTRACT

Close packed coupled multi-electrode arrays (MEA) simulating a planar electrode were used to measure the anodic current evolution as a function of position during initiation and propagation of crevice corrosion of AISI 316 stainless steel (UNS S31600) and Ni-Cr-Mo alloy 625 (UNS N06625). Scaling laws derived from polarization data guided the implementation of rescaled crevices providing spatial resolution. Crevice corrosion of AISI 316 stainless steel in 0.6 M NaCl at 50°C was found to readily initiate close to the crevice mouth (i.e., $x_{crit} \approx 0$) at modest applied potentials (e.g., $E_{app}=0 V_{SCE}$) and to spread inwards and outside the crevice with time. In the case of alloy 625, crevice corrosion initiates further inside the crevice (i.e., x_{crit} is large) and requires higher applied potential (e.g., $E_{app}=50 V_{SCE}$). The local crevice current density increased dramatically over a short period to reach a limiting value in both cases. The ramification of the larger critical depth for Ni-Cr-Mo alloys towards crevice corrosion susceptibility is also discussed.

Keywords: crevice corrosion, multi-electrode arrays, AISI 316 stainless steel, Ni-Cr-Mo alloy 625

INTRODUCTION

Crevice corrosion is currently studied using either one of two conventional techniques depending on the information required. The first method, multi crevice assembly (MCA), involves two multi-crevice formers or washers fastened on both sides of a sample sheet. This technique provides exposure information on the severity of crevice corrosion (depth, position and frequency of attack) but does not separate pitting from crevice corrosion nor provide detailed information on initiation and propagation. Moreover the MCA delivers little or no electrochemical information.¹ The second method involves the potentiodynamic or potentiostatic study of an uncreviced sample in a model crevice solution or under a crevice former in aggressive solution where crevice corrosion may initiate and propagate.² The net anodic current is monitored, an increase will signal pit or crevice corrosion depending on the experimental setup. The critical potential that triggers crevice corrosion stabilization (E_{crit}) as well as repassivation (E_{rep}) can be determined. However, crevice corrosion initiation and propagation behavior is highly dependent on the exact location in the crevice. The distance from the crevice mouth will affect the solution composition, the pH, the ohmic drop and the true potential in the crevice. These, in turn, affect the electrochemical factors controlling the reaction rate as a function of applied potential. As a result of the crevice corrosion, the solution composition, pH and the crevice ohmic drop will vary. This feedback process ultimately controls the electrochemical factors deciding the morphology and depth of attack. However the progression of these details with time is difficult to investigate using conventional crevices.

Multi-electrode arrays can provide combined spatial and temporal resolution of electrochemical properties within the crevice. A Multi-Channel Micro-Electrode Analyzer^a (MMA) has recently been used to demonstrate the interaction between localized corrosion sites (pitting corrosion and intergranular corrosion).^{3,4} Individually electrically isolated electrode elements are coupled together, through in-line zero resistance ammeters, to form a galvanically coupled electrode surface. This surface is designed to closely simulate a planar electrode surface while enabling monitoring of the current behavior of each electrode even under a crevice which would confound electrochemical probe measurements. Coupled MEAs have been successfully used in the investigation of many different corrosion phenomena: The interactions between localized corrosion sites (pitting corrosion and intergranular corrosion)^{3,4}, the lateral propagation of general corrosion on carbon steel in concrete environments⁴, and the investigation of persistent vs. switching anodes and cathodes on Cu in drinking water systems.⁴ Additionally, MEAs constructed from Al alloys and the combination of Al alloys and Cu have been used to investigate second-phase particle influences on localized corrosion⁵ and the affect of chromate conversion coatings on anode and cathode behavior.⁶ Multi electrode arrays have also been used to expedite high throughput of conventional experiments. This has been used to study the synergistic effect of large numbers of corrosion inhibitor mixtures.⁷

By coupling such a tool with crevice scaling laws derived from experimental data (a simple equation linking crevice depth/gap combinations that produces equivalent electrochemical conditions), it is possible to produce highly instrumented crevices, rescaled to enable spatial resolution of the local electrochemistry of corrosion processes.^{8,9}

^a Trade name from Scribner Associates, Inc.

Crevice corrosion is highly dependent on spatial and temporal details as expected based on different crevice corrosion stabilization models. According to Ohmic models for crevice corrosion, the potential at some position within the crevice must drop below the Flade potential E_{Flade} to stabilize crevice corrosion.¹⁰ According to chemistry change models, the solution concentration and pH must exceed critical values associated with depassivation of the initially passive alloy.¹¹

In the case of stainless steel, it has been proposed that the MnS inclusions dissolve producing thiosulfate and sulfur¹², or sulfide.¹³ When a critical concentration is reached, crevice corrosion was predicted to initiate near inclusions.¹² It has also been shown that crevice corrosion initiates at the sites of metastable pitting corrosion and that this occurs at a specific depth.^{14, 15, 16} Crevice corrosion should initiate at the depth where this critical crevice solution can be achieved. Moreover, cathodic focusing of crevice corrosion occurs at depths where the potential drops enough to enable cathodic reactions deep within the crevice to result in the absence of attack beyond a critical distance from the crevice mouth.¹⁷

The crevice depth and gap affect the solution composition, the pH, the ohmic potential drop and the true potential at any position in the crevice.¹⁸⁻²¹ These in turn affect the local anodic and cathodic current densities as a function of external potential and position during the initiation, stabilization and repassivation stages. Crevices must be rescaled in order to increase spatial resolution to utilize coupled multi-electrode arrays to shed light on these processes. Moreover, rescaled systems (with individual electrodes on the scale of tens or hundreds of micrometers) can more easily incorporate commercially available and technologically relevant alloys (often available as wire, sheet, or film) allowing for industrially meaningful experiments. FIGURE 1 (b) and (c) compares the crevice corrosion morphology obtained using a MCA to what is expected using a MEA.

While mechanistic studies of crevice corrosion of stainless steels and high performance Ni-Cr-Mo alloys have been widely available (primarily on the stainless steels)^{10-16, 22-30}, very little detailed comparison studies have been published. Those available often limit themselves to either qualitative studies, such as number of plateaus initiating crevice corrosion during multi-crevice assembly tests^{31, 32}, or they focus on single characteristic values such as the critical crevice temperature³³.

This study aims at offering a one to one comparison of crevice corrosion of alloy 625 and AISI 316 under the same conditions. It will investigate both qualitative (multi-crevice assembly test) and the quantitative aspects (multi-electrode arrays) with the goal of understanding the spatial distribution of the crevice corrosion process.

EXPERIMENTAL PROCEDURE

Scaling Laws

Scaling laws are used to rescale the crevice setup geometry while keeping the electrochemical corrosion properties similar to that of a natural crevice on a much smaller length scale. One of the advantages of rescaling is to be able to use a commercial alloy available in larger electrode sizes and, in the case of arrays, to spread the crevice corrosion over multiple single electrodes so each one of them will have a near homogeneous electrochemical behavior.

The initial step was to fit the model anodic polarization curves of stainless steel AISI 316 and alloy 625 in acid solution which simulated the crevice electrolyte. The anodic polarization

behavior of AISI 316 was determined in 0.1 M, 1 M, 2 M and 3 M HCl; alloy 625 was studied in 0.1 M, 1 M, 5.5 M and 10 M HCl. The description of the experimental setup can be found elsewhere.⁸

Using the software Crevice^{9, 17, 34} the potential and current gradient inside the crevice was calculated for various crevice gap dimensions and crevice mouth hold potentials. The chemistry inside the crevice was assumed constant and the crevice corrosion electrochemistry was assumed independent of time and space. A critical crevice depth was determined at x_{crit} , the position where the potential reaches a defined potential. It is possible to use various events to define this potential, in this case x_{crit} is found when the potential drops below the E_{Flade} . The crevice gap G combined with x_{crit} was used to generate the scaling factor x_{crit}^2/G .

Multi Electrode Array

The array is designed to simulate a flush mounted planar electrode, with 100 electrodes close-packed electrically coupled through in line zero resistance ammeters divided in ten distinctly controllable groups. The electrodes are insulated from each other by a polyimide film to avoid short circuiting. The arrays are constructed in a five by twenty formation inserted in a groove of a rod. This enables the observation of the current evolution as a function of position relative to the crevice mouth. The diameter of the electrodes (250 μm) was chosen so that x_{crit} (critical initiation distance from the crevice mouth) and the expected zone of crevice corrosion (predicted from the scaling law) would be larger than the radius of a single electrode. FIGURE 1(a) illustrates an array encased in a stainless steel rod. The arrays were assembled from polyimide coated AISI 316 stainless steel or alloy 625 electrodes to ensure electrical insulation from one another. The polyimide coating also minimized crevice attack between the coating and the electrode so that attack only initiated on polished faces. The array was mounted in a grooved rod (2.54 cm or 1" diameter). The rod was chosen as AISI 316 in the case of the stainless steel array to mimic a flush mounted planar electrode and create a creviced metallic area/total crevice area ratio close to that obtained in MCA crevices (which is 100%). The rod was made of polyformaldehyde (Delrin^b) in the case of alloy 625 due to manufacturing, economic and practical reasons. The crevice former was composed of an alloy 625 faceplate with a notch covering the array filled with polyformaldehyde to avoid short circuiting the electrodes. This setup results in a similar flush mounted effect as for the AISI 316 array. The crevice former was made of a polyformaldehyde for AISI 316 arrays. The torque applied was transferred through a two-component titanium alloy torque applicator (one convex and one concave) that resolved any planarity discrepancy as represented in FIGURE 1 (d).

The compositions of the alloys AISI 316 and 625 are given Table 1. TABLE 2 presents the critical crevice temperature (CCT), critical pitting temperature (CPT) and pitting resistance equivalent number (PREN). All of these can be used to qualitatively estimate the resistance to pitting and crevice corrosion of these alloys. The higher CCT and CPT are, the less likely crevice and pitting corrosion, respectively, will occur. Similarly, the higher the empirically derived PREN is, the less likely pitting corrosion will occur.

The arrays and crevice formers were ground and polished using SiC paper up to a 1200 grit finish. The titanium components were covered with polytetrafluoroethylene (Teflon^c) spray to reduce friction. The two components must be able to freely move one against another so

^b Trade name

^c Trade name

that the torque is homogeneously spread out. The spray promotes a more reproducible application of the set torque. The experiments consisted of long term anodic potential steps in aerated 0.6 M NaCl solution. The solution was made using reagent grade NaCl and 18.1 M Ω -cm deionized water. The samples were inserted horizontally in a flat cell opened to air with an internal coil through which hot water was circulated to maintain the solution temperature at 50°C. The reference electrode was a remotely positioned saturated calomel electrode (SCE) while the counter electrode was a platinum-coated niobium mesh. The crevice former was designed to roughly cover twelve columns of five electrodes in the case of AISI 316, leaving eight columns exposed outside the crevice former. For alloy 625, the array was fully covered as crevice corrosion was observed to initiate deeper inside the crevice based on preliminary experiments. A few drops of solution were applied on the array before tightening the crevice former so that solution is present within the crevice from the beginning of the test (the torque used was 2.84 N-m/25 inch-lbs).

Verification that the coupled MEA behaves similarly to planar electrodes was confirmed by comparing anodic polarization data from MCA samples to the anodic polarization of the array for both AISI 316 and alloy 625. The crevice former for the MCA electrode was made of Polyformaldehyde, with both the sample and the crevice former ground using SiC paper up to 1200 grit. For AISI 316 MCA, the potential was swept from -0.1 V vs. open circuit potential (V_{OCP}) to 0.6 V_{SCE} or 0.15 V_{SCE} (to reduce the pitting corrosion at uncreviced sites) at a scan rate of 0.1667 mV.sec⁻¹. For alloy 625, the vertex potential was chosen to be 1 V_{SCE} . The potential was then swept back to -0.1 V_{OCP} at the same rate. The creviced planar electrode experiments were performed in 0.6 M NaCl at 50°C. MEA experiments were performed in aerated 0.6 M NaCl at 50°C. The potential was swept from -0.1 V_{OCP} to 0.7 V_{SCE} at a scan rate of 0.1 mV.sec⁻¹, and held at that potential for one hour. The potential was then swept back to -0.1 V_{OCP} at the same rate.

For long term crevice corrosion tests, the creviced arrays were immersed in the heated solution for two days at open circuit potential to allow for passive film growth and solution wicking into the whole crevice. The uncovered parts of the rod and the array (for AISI 316 array), and the crevice former (for alloy 625) were kept at a potential within the passive range in order to avoid extensive pitting corrosion outside the crevice. Those applied passive potentials were -25 mV_{SCE} and 0 V_{SCE} for AISI 316 and alloy 625, respectively. The starting scan potentials were chosen to be -25 mV_{SCE} and 50 mV_{SCE} for AISI 316 and alloy 625, respectively. The creviced array potential was increased by 25 mV increments every 24 hours (equivalent to 3.10⁻⁴ mV.sec⁻¹) to favor crevice corrosion over pitting corrosion. The experiments were terminated at 25 mV_{SCE} for AISI 316 and at 75 mV_{SCE} for alloy 625; these values were chosen during the experiment according to the extent of crevice corrosion observed.

RESULTS

Scaling Laws

Scaling laws were derived from anodic polarization data obtained in acid solution that mimic the acidified pH of crevice solutions. FIGURE 2 (a) and (b) shows experimental anodic polarization curves for AISI 316 and alloy 625 microelectrodes (250 μm diameter), respectively, in various HCl concentrations. The AISI 316 becomes uniformly active in all solutions except for 0.1 M HCl where pitting occurred. In contrast alloy 625 exhibits an active-passive transition in solutions as aggressive as 5.5 M HCl.

The potential and current density profile inside crevices of a given gap were calculated at different crevice gaps for various applied potentials using Crevice. x_{crit} is defined as the distance from the crevice mouth to the site where the local potential E reaches the Flade potential (E_{Flade}). For AISI 316 assuming a 1M HCl crevice solution at ambient temperature, E_{Flade} is $-0.2 V_{SCE}$ (from FIGURE 3 (c)). In the case of alloy 625 assuming a 2M HCl crevice solution at $60^{\circ}C$, the E_{Flade} is $-0.135 V_{SCE}$ (from FIGURE 3 (d)). The current density distributions in a crevice for AISI 316 assuming a 1 M HCl crevice solution at ambient temperature, a crevice gap of 3 microns and various crevice mouth hold potentials are shown in FIGURE 3 (a). The shaded vertical columns represent the physical position of the electrodes in an array with the same dimensions as the one described previously. Positions of severe crevice corrosion can be predicted based on current maximums. For AISI 316 these are found at the mouth and starting from the fourth or the sixth electrode (0.625-2 mm from the crevice mouth) over a range of five electrodes for external hold potentials of $0.2 V_{SCE}$ and $0.4 V_{SCE}$, respectively. For an external potential held at $-50 mV_{SCE}$ and $25 mV_{SCE}$, severe crevice corrosion will only be observed between the third or the fifth electrode and deeper. It is noteworthy that the higher the crevice mouth applied potential (E_{app}) is, the higher the current density is at the mouth, resulting in a very localized attack zone at the mouth in the case of AISI 316. FIGURE 3 (b) presents the current density gradient in the crevice for alloy 625 assuming a solution of 2 M HCl at $60^{\circ}C$ with a crevice gap of 3 microns. The higher current densities can be found at a distance from the 5th wire to the 12th wire with no maxima at the mouth. The higher the applied potential is the deeper i_{peak} (maximum current density) can be found. However, i_{peak} does not vary with E_{app} . FIGURE 4 (a) and (b) shows the evolution of the potential under the crevice with the distance from the crevice mouth for various crevice gaps. The potential gradients were again modeled for AISI 316 assuming a 1 M HCl solution at ambient temperature and for a 2 M HCl solution at $60^{\circ}C$ for alloy 625. The potential distribution spreads out as the gap is increased from 0.1 to 30 μm . In fact at 0.1 μm , all potential drops would occur on the first few electrodes of the array.

The depth into the crevice at which the local potential dropped to E_{Flade} was termed the x_{crit} value. It could be determined for each gap from FIGURE 4 (a) and (b). Replicating this process for various crevice gaps (G) it is possible to obtain a “family” of x_{crit}^2/G values as a function of gap. These in turn can be plotted linearly as x_{crit}^2 vs. G as shown FIGURE 5 (a) and (b) for AISI 316 and alloy 625, respectively. The horizontal bars represent the physical position of the electrodes of the array relative to the crevice mouth. The shaded areas in FIGURE 5 (a) represent the position where the current density is above $6 \cdot 10^{-4} A \cdot cm^{-2}$ when the crevice mouth hold potential (E_H) is $0.2 V_{SCE}$. The scaling laws predict that crevice attack would be closer to the mouth for AISI 316 than for alloy 625 if the solution inside the crevice is described by electrochemical kinetics similar to those observed in 1 M HCl at ambient temperature for AISI 316 and 2 M HCl at $60^{\circ}C$ for alloy 625. A high current density area exists close to the crevice mouth for AISI 316, this is related to the high E_{app} and the active polarization behavior at high potential as observed in FIGURE 3 (a).

If during the course of crevice corrosion the solution becomes more aggressive than 1 M HCl (e.g., note the E-I behavior of AISI 316 with 3 M HCl), E_{Flade} might not be observed in the E-log(i) behavior (see FIGURE 2 (a)) and then crevice attack becomes greatest at the mouth where the IR drop is lowest.

Planar Creviced Electrode vs. Coupled Multi-Electrode Array

The crevice corrosion initiation potential (E_{crit}) and repassivation potential (E_{rep}) were determined for all the electrodes in the MEA configuration covered by the crevice former during

the potential sweep test. The average of E_{crit} and E_{rep} of the five rows located at a given depth into the crevice was calculated and the standard deviation was determined. These values are shown, as a function of the distance from the crevice mouth along with the position independent E_{crit} and E_{rep} data from planar electrode tests on MCA samples in FIGURE 6 (a) for AISI 316 and FIGURE 6 (b) for alloy 625. The extents of attack after the MCA tests are presented FIGURE 6 (c) for AISI 316 (using a vertex potential of $0.6 V_{SCE}$) and FIGURE 6 (d) for alloy 625. Both pictures are accompanied by that of a single plateau. Note that corrosion spreads well outside the crevice in the case of AISI 316 but is within the position of the crevice former in the case of alloy 625. The depth x_{crit} is difficult to ascertain because of the tight gap in the MCA. To confirm that the crevice corrosion behavior of the array is similar to that of the MCA sample, the critical potential of the first electrode that initiates crevice corrosion on the array should be equivalent to E_{crit} for the creviced planar electrodes. Similarly, the last electrode to repassivate should do so at a potential that is close to the repassivation potential of the MCA samples. It can be seen in FIGURE 6 (a) that the first three electrode positions displayed E_{crit} and E_{rep} values very close to those found for tests with the planar electrode. In FIGURE 6 (b), for alloy 625, the critical and repassivation potential (E_{crit} and E_{rep} , respectively) of the array were found to be close to those found for the MCA. Discrepancies between E_{crit} and E_{rep} for MCA and MEA can be explained by the position dependent values for the ohmic drop inside the crevice. Indeed, as the distance increases, the resistance of the crevice solution away from the crevice mouth also increases, therefore the potential applied at the mouth needed for crevice corrosion to initiate further from the mouth is higher.

Long Term Crevice Corrosion of MEA

FIGURE 7 (a) and (b) shows current maps of the controlled coupled multi-electrode array of AISI 316 and alloy 625, respectively during long term experiments conducted in 0.6 M NaCl at $50^{\circ}C$ with rescaled MEAs. The bold line between columns 13 and 14 for AISI 316 and to the right of column 18 for alloy 625 shows the crevice mouth position. The area under the crevice is on the left of this line.

Crevice corrosion initiated after five hours at $0 V_{SCE}$ on electrodes B11 and B12 (second and third electrodes from the crevice mouth) for AISI 316. Two hours after initiation, crevice corrosion propagated closer to the crevice mouth (column 13) and further inside (column 10) as well as sideways (row D and E). This suggests that an aggressive environment similar to 3 M HCl appeared. The current density will reach high values close to the crevice mouth when the solution acidifies to the point where no active-passive transition is observed. Over the next three current maps (9 hrs, 11 hrs and 13 hrs) both depth and lateral spreading of crevice attack was observed as well as corrosion outside the mouth. All electrodes in columns 10 to 13 have significant crevice attack after 13 hours at $0 V_{SCE}$. The last map represents the current densities of the array at the end of the test (i.e. after an extra 24 hours at $25 mV_{SCE}$). The current map shows that crevice corrosion spreads away from the crevice mouth. Additionally, pitting corrosion is found initiating on six electrodes outside of the crevice former (on columns 14, 15 and 16). In the case of alloy 625, crevice corrosion initiated after 18 hours at $50 mV_{SCE}$ at position C6. Over the next six hours, the crevice corrosion spread over the four closest columns.

FIGURE 8 shows the full mounted AISI 316 array as well as a blown up image of the 5×20 electrode array after the entire stepped potentiostatic test. The solid gray line represents the position of the crevice mouth. The light gray electrodes are slightly attacked while the dark gray electrodes closer to the mouth suffer deeper attack. The dark gray and black electrodes further from the crevice mouth are unattacked sites and the dark aspect is due to the polished

finish that is still present (the same color can be observed on the bold area of the mounting rod). The corroded electrodes can be related to the current density map at the end of the experiment, shown in FIGURE 7 (a). The potential was increased to 25 mV_{SCE} inside the crevice for 1 day after 24 hours at 0 V_{SCE}. Crevice corrosion spread further inside once the potential increased as observed by the larger number of anodically polarized electrodes in the last map of FIGURE 7 (a). FIGURE 8 also shows the effect of crevice corrosion on the stainless steel rod.

It is possible to derive the net depth of attack from the net anodic currents measured for each position under the crevice. Assuming that the depth of attack is homogeneous over the whole surface of a single electrode and that local cathode currents are small (hence $i_{\text{net}} \approx i_{\text{anodic}}$), the total depth of attack $d(T)$ at a time T can be derived from equation (1), with EW_{316} being the equivalent weight assuming congruent dissolution of AISI 316 stainless steel, F the Faraday constant, ρ_{316} the density of AISI 316 stainless steel, r the radius of the electrode, $I(t)$ the current at a time t , dt the time interval between each measurement and t_0 the initiation time. The same equation can be applied to alloy 625 using EW_{625} instead of EW_{316} and ρ_{625} instead of ρ_{316} (the values of EW_{316} , EW_{625} , ρ_{316} and ρ_{625} can be found in Table 2).

$$d(T) = \frac{EW_{316}}{F\rho_{316}\pi r^2} \int_{t=t_0}^{t=T} I(t)dt \quad (1)$$

FIGURE 9 (a) and (b) shows the evolution of the calculated depth of attack of all electrodes of a selected row for AISI 316 and alloy 625, respectively. A succession of depth profiles derived as a function of crevice depth from the current data using equation (1) at various exposure times are shown FIGURE 10 (a) and (b) for AISI 316 and alloy 625, respectively. The interval between each curve is fifty minutes. The crevice mouth is represented by a vertical dashed line in FIGURE 10 (a). For AISI 316 the corrosion depth near the mouth is much higher while it decreases with the distance from the crevice mouth. Note that the maximum depth of attack derived is small compared to the electrode diameter. This eliminates the concern of formation of a “lead-in-pencil” electrode configuration on individual electrodes (i.e., a one-dimension pit equivalent to a sub-crevice created by a wire electrode under the flat crevice former). In the case of alloy 625, the majority of the electrodes exhibit depth of attack lower than those observed for AISI 316. Most of the electrodes also display a plateau after a fast penetration rate; this plateau is representative of the repassivation of the electrodes. The two deepest attacked electrodes are not close to each other (C6 and C11). This can also be observed on the current maps shown in FIGURE 7 (b). Over the course of the first 18 hours, various electrodes can be seen to initiate and repassivate apparently randomly. This is thought to be due to localized crevice corrosion activity that could result from a variable crevice gap, as when the tighter the crevice gap is, the lower E_{crit} (critical crevice potential) will be. Stable crevice corrosion is found to initiate after 18 hours at 50 mV_{SCE}. Alloy 625 is confirmed as being more corrosion resistant than AISI 316 as the critical crevice potential is found to be higher (50 mV_{SCE} instead of 0 V_{SCE}, respectively, at 50°C in 0.6 M NaCl). Also, the active electrodes observed after crevice corrosion initiation of alloy 625 tend to repassivate

unlike AISI 316. Finally, except for two electrodes, the derived depth of attack for AISI 316 is larger by at least one order of magnitude than for alloy 625.

DISCUSSION

Scaling Laws

Considering a similar solution (1M HCl at ambient temperature for AISI 316 and 2M HCl at 60°C for alloy 625) with the same applied potential of 0.2 V_{SCE} , it can be observed that the slope of x_{crit}^2 vs. G found for the scaling law of alloy 625 is steeper than for that of AISI 316, see FIGURE 5 (a) and (b) for the scaling laws of AISI 316 and alloy 625, respectively. This is explained partly by the anodic polarization behavior of both metals. Considering a model crevice solution of 1 M HCl at ambient temperature (see FIGURE 2 (a) and (b)), at a given potential of 0.1 V_{SCE} , AISI 316 displays an active behavior. For the same conditions, alloy 625 shows an active passive transition and at an applied potential of 0.2 V_{SCE} , the behavior will be passive, therefore an ohmic drop is necessary to reach E_{Flade} and therefore to activate crevice corrosion. This needed ohmic drop means that crevice corrosion initiation will occur at a distance from the crevice mouth. Consequently, assuming similar crevice solutions, crevice corrosion will initiate further away from the crevice for alloy 625 than for AISI 316. FIGURE 5 (a) and (b) show that by assuming a crevice gap of four microns in the rescaled crevice, the x_{crit} position (for $E_{crit}=E_{Flade}$) can be found to be on the eighth electrode from the crevice mouth in the case of the AISI 316 array (approximately 2.2 mm). For alloy 625, in similar conditions and with the same gap, x_{crit} is found on the twelfth electrode from the crevice (about 3.6 mm).

The scaling laws for alloy 625 are derived based on anodic polarization behavior in 2M HCl at 60°C, compared to 1 M HCl at ambient temperature for AISI 316. This environment change only reduces the difference in x^2/G scaling law relationships. Indeed, for alloy 625 higher pH solution at lower temperature will only tend to push its anodic behavior towards passivity, i.e. no more mass transport limited behavior, decrease of the passive current density, decrease of the maximum current density (i_{peak}) during the active-passive transition and most importantly, decreased E_{Flade} . Therefore the value of x_{crit} will increase further when the pH is increased and the temperature is decreased. The x^2 vs. G relationship of alloy 625 in 1 M HCl at ambient temperature (i.e. same conditions as for the calculated AISI 316 scaling law) will be expected to have a steeper slope and the difference between AISI 316 and alloy 625 will increase.

A variation of the applied potential at the mouth will also affect the position of x_{crit} . This can be observed on FIGURE 3 (a) for AISI 316 and (b) for alloy 625. The position of i_{peak} is found to shift further inside as the applied potential is increased because a greater ohmic voltage is required to decrease the potential to E_{Flade} . It can also be noted that the maximum current does not increase with the applied potential assuming a fixed solution concentration in the crevice. Therefore, the extent of attack can be predicted to be similar while only the position changes. This is explained by the anodic polarization behavior of AISI 316 and alloy 625 (See FIGURE 3 (c) and (d), respectively). i_{peak} increases or decreases if the crevice solution pH decrease or increase, respectively (see FIGURE 2 (a) and (b)). The effect of the applied potential on the scaling laws can also be observed in FIGURE 5 (b) for alloy 625 as an example. The slope of x_{crit}^2 vs. G relationship increases with the applied potential for the reason explained earlier. FIGURE 3 (a) also displays an increase in current density close to the crevice mouth as the applied potential for AISI 316 goes from passive to active. The shaded areas in FIGURE 5 (a) represent the zones where the current density is above $6 \cdot 10^{-4}$ A.cm⁻². While the main zone of attack is found along the x_{crit}^2 vs. G line, another one exists

close to the crevice mouth ($x = 0$ position). The latter zone is due to the current density increase observed in FIGURE 3 (a). As the crevice gap increases the width of both zones (on the x_{crit} axis) increases.

Planar Creviced Electrode vs. Multi Electrode Array

The critical and repassivation potential for the multi crevice assembly of alloy 625 and AISI 316 have been determined as the potential for which the current density reaches 10^{-6} A.cm⁻². In the case of the MEA, the critical potential is defined as the potential for which the current density exceeds $2 \cdot 10^{-4}$ A.cm⁻² while for the repassivation potential, the critical current density is chosen to be $1 \cdot 10^{-4}$ A.cm⁻². The critical and repassivation potentials for AISI 316 MEA are found to be very close to those of the MCA. However they increase with the distance from the crevice mouth. This could be explained by the ohmic drop found in the crevice. FIGURE 3 (a) demonstrates this explanation; as the applied potential is increased, x_{crit} increases. Therefore, for crevice corrosion to initiate further inside the crevice (i.e., to increase x_{crit}), the applied potential must be increased. For alloy 625, the first electrode to initiate crevice corrosion does so at a potential equal to the MCA critical potential. Similarly, the last alloy 625 MEA electrode repassivates at a potential close to the MCA repassivation potential. Thus, the MEA yields results similar to a conventional electrode.

Not only are MCA and MMA results consistent with each other, from a threshold potential stand point, they are also consistent considering the extent of damage and the damage location. For AISI 316, attack proceeds beyond the mouth. For alloy 625, attack is confined under the crevice. For the MCA, the crevice gap is so tight, that the x_{crit} is too small to identify.

Long Term Crevice Corrosion of MEA

Crevice corrosion was found to initiate further from the crevice mouth for alloy 625 than for AISI 316 (see FIGURE 7 (a) and (b) for AISI 316 and alloy 625, respectively). This follows the prediction made by using the scaling laws. The distance between the initiation position for AISI 316 and alloy 625 was also found to be qualitatively similar but greater than what was predicted with the scaling laws, FIGURE 5. The same conditions used for the long term corrosion experiments (temperature, bulk solution composition) accentuate the difference between the positions of initiation as explained previously.

By the end of the step following initiation (25 mV_{SCE} for AISI 316), crevice corrosion spreads inwards for AISI 316, see FIGURE 7 (a). The current density of some electrodes outside the crevice becomes highly anodic. This can be explained by the diffusion of the aggressive crevice solution (low pH, high chloride content) to positions outside of the crevice coupled with the poor resistance of AISI 316 to more dilute HCl solutions. FIGURE 2 (a) presents the anodic behavior of AISI 316 and shows clearly that the dilute acidic crevice solution diffusing from the mouth will depassivate the outside electrodes. The acidity of the outside solution will decrease with the distance from the crevice mouth due to dilution into the bulk solution. Therefore, the corrosion is limited to a zone close to the crevice mouth.

It is interesting to note that corrosion outside the crevice mouth will not be expected for alloy 625, indeed FIGURE 2 (b) shows that alloy 625 displays a passive behavior with an active-passive zone even in very acidic solution. Crevice corrosion can be expected for alloy 625 in 0.6 M NaCl at 50°C at high enough applied potential due to the combination of IR drop and low pH. However pitting corrosion due to crevice solution leaking is highly unlikely. This was also observed during the MCA test, shown in FIGURE 6 (d). On the other hand, the same

MCA experiments have shown that AISI 316 will suffer both crevice and pitting corrosion, see FIGURE 6 (c), with the latter affecting the uncreviced sample.

FIGURE 9 (a) shows that the closer the electrodes are to the crevice mouth, for AISI 316, the higher the current densities are and consequently, the deeper the attack is. The currents increase dramatically during the beginning of the crevice corrosion, as shown by the high depth vs. time slope. They then quickly reduce to much lower currents resulting in a much slower penetration rate. Similar and more extreme behavior is found for alloy 625, FIGURE 9 (b); observing row C, only two electrodes present signs of deep attack. The rest of the row will either stay passive or present a metastable or stable localized corrosion behavior. Electrodes such as C10 will exhibit a brief burst of activity resulting in a steep depth slope and very quickly repassivate (which is shown by a constant depth value plateau). On the other hand, electrode C11 exhibits a much deeper attack that does not repassivate.

The distribution of attack for alloy 625 is not as clearly defined as for AISI 316. In FIGURE 7(b), after 10 hours at 50 mV_{SCE} multiple single non-adjacent active sites can be observed. Only after 18 hours do some anodic sites begin to initiate proximate to others (column 5, 6 and 7). This anodic zone spreads over the contiguous columns over time as crevice corrosion. Therefore, we can differentiate the localized activities with high anodic current (such as electrode C6 and C11) from crevice corrosion. By assuming such a difference, we can conclude that the depth of the crevice corrosion attack of alloy 625 is much shallower than for AISI 316. Furthermore, its location is farther from the crevice for alloy 625 than for AISI 316.

FIGURE 10 (a) and (b) show derived depth cross-sections at intervals of 50 minutes for AISI 316 and alloy 625, respectively. It is clear for AISI 316 that the depth increases progressively, closer to the crevice mouth. The corrosion depth of attack observed outside the crevice mouth is much deeper than that found within the crevice. For alloy 625, at 50 mV_{SCE} (in black), the depth of attack on C11 and C6 is so large that it dwarves the depth for crevice corrosion (C3 to C7). At 75 mV_{SCE} (in grey) electrodes C11 and C6 still display much deeper depth of attack but an apparently homogeneous background can be seen from C2 to C15. The area displaying crevice corrosion is increasing because, because the solution is expected to become more aggressive as the potential increases. This corresponds to the crevice corrosion zone of attack observed on the last current density map in FIGURE 7 (b).

Anticipated Crevice Corrosion of Ni-Cr-Mo alloys

Knowing the anodic polarization behavior of an alloy it is possible to gain insight into its crevice corrosion behavior as displayed by the Crevicer results presented previously (FIGURE 3, FIGURE 4 and FIGURE 5). By knowing the shape of E-I anodic behavior and current density magnitude it is possible to predict the position of the attack for the assumed conditions, whether the position is at the crevice mouth or within the crevice at depth. FIGURE 11 (a) presents the i_{peak} for AISI 316 and alloy 625 as well as i_{peak} for a selection of model Ni-Cr-Mo alloys (Ni-22Cr-xMo, with x=0, 3, 6, 9 and 13 wt%) for various HCl concentrations at ambient temperature. All alloys except for Ni-22Cr are passive in 0.1 M HCl. This would mean that if the critical crevice solution is equivalent in pH and chloride content to 0.1 M HCl, these alloys would not suffer crevice corrosion. In 1 M HCl, with the exception of Ni-22Cr-9Mo and Ni-22Cr-13Mo, all alloys display an active passive transition. As E_{flade} increases, the crevice corrosion initiation site will move closer to the crevice mouth assuming that the applied potential at the mouth is constant. Once the Flade potential is above the applied potential or does not exist (either due to active behavior or mass transport limited behavior), crevice corrosion will only be

found at the mouth. Therefore, from FIGURE 11 (a), in 1 M HCl solution, we can predict that the position of crevice corrosion (i.e., x_{crit}) will get deeper in the following order: Ni-22Cr, AISI 316, Ni-22Cr-3Mo, Ni-22Cr-6Mo and alloy 625. The presence of alloy 625 between Ni-22Cr-6Mo and Ni-22Cr-9Mo is expected as alloy 625 contains 20 to 23 wt% of Cr and 8 to 10 wt% of Mo, ranking it within the vicinity of Ni-22Cr-9Mo. Ni-22Cr-9Mo and Ni-22Cr-13Mo are still passive in 1M HCl and therefore will not exhibit signs of crevice corrosion. Ni-22Cr-13Mo can be related in Cr and Mo content to alloy 22 in the same way than Ni-22Cr-9Mo is similar to alloy 625. Multiple studies have shown the better resistance to crevice corrosion of alloy 22 when compared to alloy 625.^{14, 16, 24, 25, 27, 33}

While i_{peak} only provides information concerning the extent of attack, the Flade potential provides important clarifications regarding the position of crevice corrosion. For a fixed applied potential, as explained previously, the larger E_{Flade} is, the closer to the mouth will crevice corrosion be. FIGURE 11 (b) presents the evolution of E_{Flade} for alloy 625 in HCl solutions of various concentrations. E_{Flade} increases with the HCl concentration. Therefore, crevice corrosion will increase closer to the mouth as the pH of the crevice solution decreases. Another factor that will affect the location of crevice corrosion is the value of i_{peak} relative to $i_{passive}$. Regarding this issue, FIGURE 11(b) also presents the evolution of i_{peak} , $i_{passive}$ and Δi with $\Delta i = i_{peak} - i_{passive}$. The larger Δi is the deeper crevice corrosion will occur as the extra current density will also affect the IR drop controlling the location of crevice corrosion. As the HCl concentration increases, Δi also increases and therefore the crevice corrosion location will be shifted further away from the crevice mouth. It is also interesting to note that when x_{crit} is larger than the physical size of the crevice former, crevice corrosion is not possible; this is of interest especially in the case of small natural crevice formers and the use of alloys like C22 with low Flade potentials. These issues will be developed in future works.

CONCLUSION

The MEA has been shown to be useful in the study of crevice corrosion providing spatially and temporally resolved electrochemical measurements of crevice attack. The comparison of critical and repassivation potentials with data from planar crevice electrode tests of similar material reveal that the MEA behaves similarly to a planar sample. Scaling laws derived from anodic polarization data offer model x_{crit}^2 vs. G relationships that enable rescaling of the crevice geometry to the larger-scale dimensions of the MEA. Long step potential tests permit the study of the initiation and growth of crevice corrosion. Crevice corrosion on AISI 316 stainless steel in 0.6 M NaCl at 50°C was found to initiate at a potential of 0 mV_{SCE} under the crevice but near the mouth. For alloy 625, exposed under the same conditions, crevice corrosion initiated further inside the crevice at 50 mV_{SCE}. The position of the initiation was found to be consistent with the predictions based on scaling laws developed in simulated crevice solutions. From the current measured, the depth of attack evolution with time can be derived. For AISI 316, the further the electrode is from the crevice mouth, the later it initiated and the lower the maximum current was. In the case of alloy 625, the spatial distribution of depth of attack was not as systematic about the mouth as in the case of AISI 316. The depth values obtained (1-50 μm) are consistent with the visual results. The insight on crevice corrosion suggests that if $E_{Flade} > E_{app}$ crevice corrosion occurs at the mouth. However, if E_{Flade} is lower than E_{app} and if the IR drop inside the crevice is significant enough, crevice corrosion will initiate at a fixed distance from the crevice mouth (i.e., x_{crit}) depending on the crevice solution composition and pH. If E_{Flade} is too low or inexistent, then crevice corrosion will be avoided. These results imply that certain combinations of E_{Flade} , E_{app} and $x < x_{crit}$ lead to avoidance of crevice corrosion.

ACKNOWLEDGEMENTS

Support by the Science & Technology Program of the Office of the Chief Scientist (OCS), Office of Civilian Radioactive Waste Management (OCRWM), U.S. Department of Energy (DOE), is gratefully acknowledged. The work was performed under the Corrosion and Materials Performance Cooperative, DOE Cooperative Agreement Number: DE-FC28-04RW12252. The views, opinions, findings, and conclusions or recommendations of authors expressed herein do not necessarily state or reflect those of the DOE/OCRWM/OCS.

REFERENCES

1. G 78-01: Standard Guide for Crevice Corrosion Testing of Iron-Base and Nickel-Base Stainless Alloys in Seawater and Other Chloride-Containing Aqueous Environments, in *Annual Book of ASTM Standards*, ASTM, (2003).
2. G 61-86: Standard Test Method for Conducting Cyclic Potentiodynamic Polarization Measurements for Localized Corrosion Susceptibility of Iron-, Nickel-, or Cobalt-Based Alloys, in *Annual Book of ASTM Standards*, ASTM, (2003).
3. N. D. Budiansky, J. L. Hudson and J. R. Scully, *J. Electrochem. Soc.* , **151**, B233 (2004).
4. N. D. Budiansky, F. Bocher, H. Cong, M. F. Hurley and J. R. Scully, in *Corrosion NACEExpo 06*, Paper 06677, San Diego,(2006).
5. F. D. Wall, M. A. Martinez, C. M. Johnson, J. C. Barbour, N. Missert and R. G. Copeland, in *Symposium on Corrosion and Protection of Light Metal Alloys held at 204th Meeting of the Electrochemical Society*, T. E. Society Editor p. 1, The Electrochemical Society, (2004).
6. W. Zhang, B. Hurley and R. G. Buchheit, *J. Electrochem. Soc.* , B357 (2002).
7. B. D. Chambers and S. R. Taylor, in *Corrosion NACEExpo 06*, Paper 06678, San Diego,(2006).
8. F. Bocher, F. Presuel-Moreno, N. D. Budiansky and J. R. Scully, *Electrochemical and Solid-State Letters*, (2006). accepted
9. J. S. Lee, M. L. Reed and R. G. Kelly, *J. Electrochem. Soc.* , **151**, B423 (2004).
10. H. W. Pickering, in *Localized Corrosion, CORROSION/Research Topical Symposium Proceedings*, J. R. Scully and G. S. Frankel Editors, p. 103, NACE, (2001).
11. J. W. Oldfield and J. W. Sutton, *British Corrosion Journal*, **13**, 13 (1978).
12. S. E. Lott and R. C. Alkire, *J. Electrochem. Soc.* , **136**, 973 (1989).
13. C. S. Brossia and R. G. Kelly, in *Critical Factors in Localized Corrosion II*, P. M. Natishan, R. G. Kelly, G. S. Frankel and R. C. Newman Editors, p. 201, Pennington NJ, The Electrochemical Society, (1995).
14. B. A. Kehler, G. O. Ilevbare and J. R. Scully, in *Localized Corrosion, CORROSION/Research Topical Symposium Proceedings*, J. R. Scully and G. S. Frankel Editors, p. 30, NACE,

(2001).

15. N. J. Laycock, J. Stewart and R. C. Newman, *Corros. Sci.*, **39**, 1791 (1997).
16. B. A. Kehler and J. R. Scully, *Corrosion*, **61**, 665 (2005).
17. K. C. Stewart, Intermediate Attack in Crevice Corrosion by Cathodic Focusing, PhD Dissertation, in *Materials Science and Engineering*, University of Virginia, Charlottesville, VA (1999).
18. M. I. Abdulsalam and H. W. Pickering, *Corros. Sci.*, **41**, 351 (1998).
19. J. R. Kearns, Crevice, in *Corrosion Tests and Standards: Application and Interpretation*, R. Baboian Editor p. 175, ASTM, (1995).
20. R. G. Kelly, Crevice Corrosion, in *ASM Handbook Vol. 13A Corrosion: Fundamentals, Testing, and Protection*, p. 242, ASM, (2003).
21. A. J. Sedriks, Crevice Corrosion, in *Corrosion of Stainless Steel*, 2nd ed., p. 176, Wiley Interscience, (1996).
22. C. S. Brossia and R. G. Kelly, *Corros. Sci.*, **40**, 1851 (1998).
23. C. S. Brossia and R. G. Kelly, *Corrosion*, **54**, 145 (1998).
24. B. A. Kehler, Crevice Corrosion Electrochemistry of Alloys 625 & C22, in *Materials Science and Engineering*, University of Virginia, Charlottesville, VA (2001).
25. B. A. Kehler, G. O. Ilevbare and J. R. Scully, *Corrosion*, **58**, 1042 (2001).
26. R. S. Lillard, M. P. Jurinski and J. R. Scully, *Corrosion*, **50**, 251 (1994).
27. F. J. Martin, P. M. Natishan, K. E. Lucas, E. A. Hogan, A. M. Grolleau and E. D. Thomas, *Corrosion*, **59**, 498 (2003).
28. J. W. Oldfield, *Corrosion*, **46**, 574 (1990).
29. R. B. Rebak, in *Corrosion 2005*, Paper 05457, Houston, Tx, USA, NACE, (2005).
30. G. Salamat, G. A. Juhl and R. G. Kelly, *Corrosion*, **51**, 826 (1995).
31. M. A. Streicher, *Materials Performance*, 37 (1983).
32. H. P. Hack, in *NACE*, Paper 65, Houston, Tx, NACE, (1982).
33. Haynes International, Hastelloy C-22 Alloy Manufacturer Brochure, H-2019F
34. Crevice website, in <http://www.virginia.edu/cese/research/crevice.html>, (2002).

TABLE 1. COMPOSITION RANGE OF AISI 316 (UNS NO. S31600) AND ALLOY 625 (UNS NO. N06625) IN WT. %

	Al	C	Cb	Cr	Fe	Mn	Mo	Ni	P	S	Si	Ta	Ti
316	0	<0.03	0	16-18.5	Bal.	<2	2-3	10-14	<0.045	<0.03	<1	0	0
625	<0.4	<0.01	3.15-4.15	20-23	<5	<0.015	8-10	Bal.	<0.015	<0.015	<0.5	<0.05	<0.4

TABLE 2. CHARACTERISTIC VALUES FOR AISI 316 AND ALLOY 625. CRITICAL CREVICE TEMPERATURE (CCT), CRITICAL PITTING TEMPERATURE (CPT)³³, PITTING RESISTANCE EQUIVALENT NUMBER (PREN= $CR\%WT+3.3*MO\%WT+16*N\%WT$), DENSITY ρ AND EQUIVALENT WEIGHT EW (ASSUMING CONGRUENT DISSOLUTION).

	CCT (°C)	CPT (°C)	PREN	EW (g.equivalent ⁻¹)	ρ (g.cm ⁻³)
316	<5	20	25.5	25.4	7.87
625	50	90	51.7	26.7	8.44

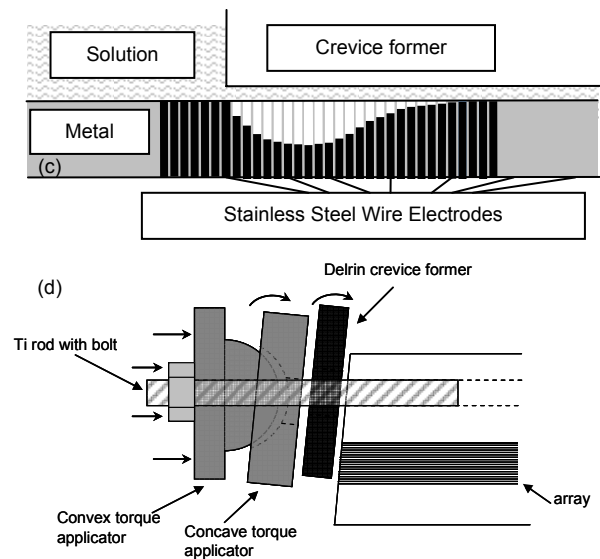
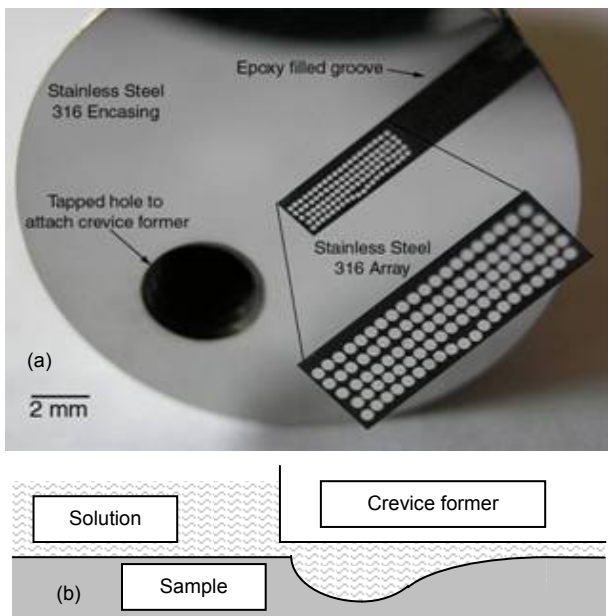


FIGURE 1. (a) Close packed array of one hundred AISI 316 stainless steel electrodes (250 μ m diameter) in 5*20 arrangement mounted in AISI 316 stainless steel rod. (b) Schematic representation of crevice corrosion attack of a planar sample. (c) Schematic representation of multi-electrode array. (d) Schematic representation of the crevice former device.

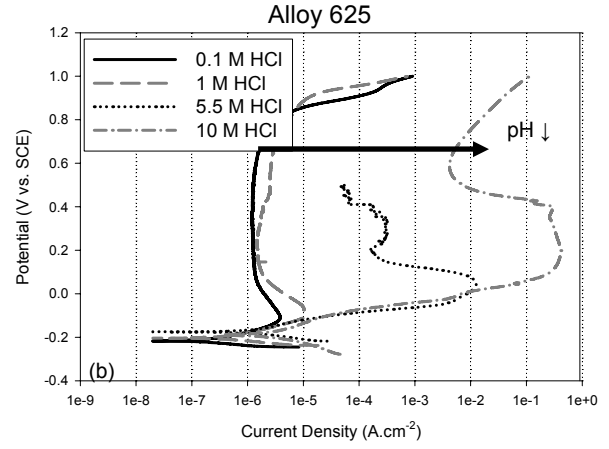
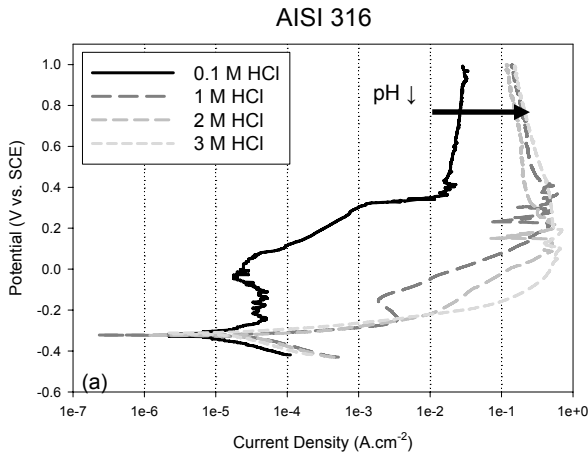


FIGURE 2. Anodic polarization behavior in various HCl concentrations at ambient temperature under deaerated conditions for (a) AISI 316 and (b) Alloy 625

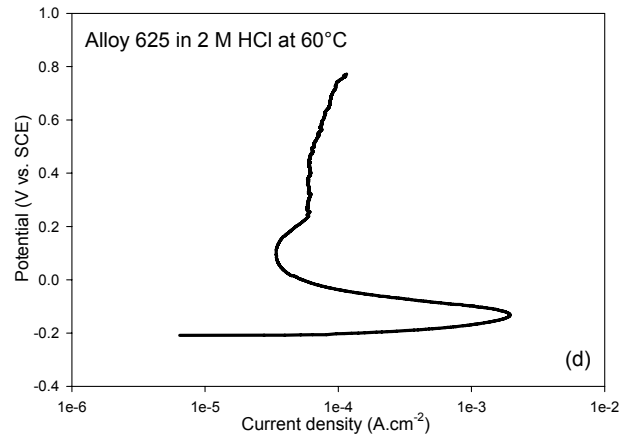
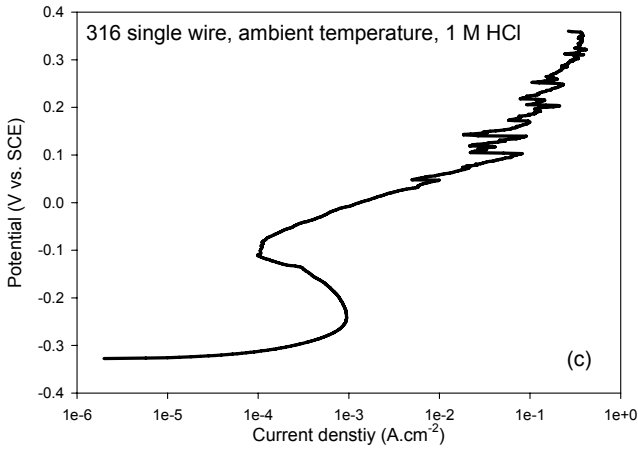
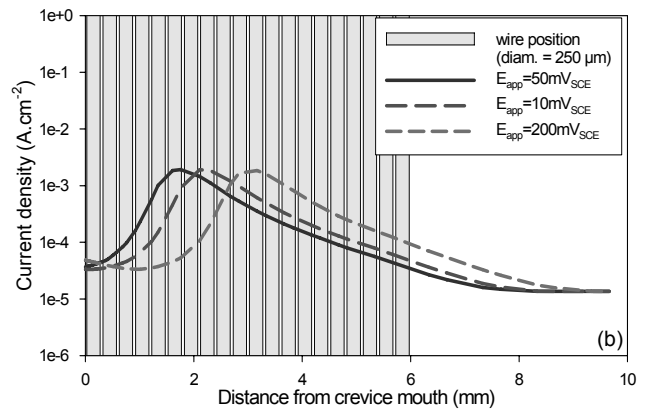
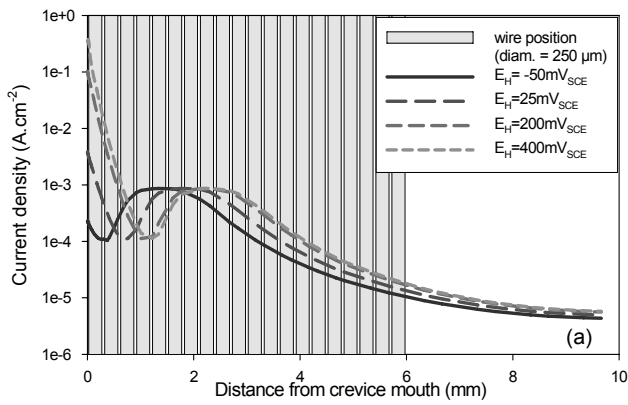


FIGURE 3. Evolution of the current density with the distance from the crevice mouth at various applied potential at the mouth for (a) AISI 316 in 1 M HCl at ambient temperature assuming a 3 micron crevice gap and (b) Alloy 625 in 2 M HCl at 60°C assuming a 3 micron crevice gap. The anodic polarization behavior used as basis for the modeling of the current and potential gradient of (c) AISI 316 and (d) Alloy 625 are also shown.

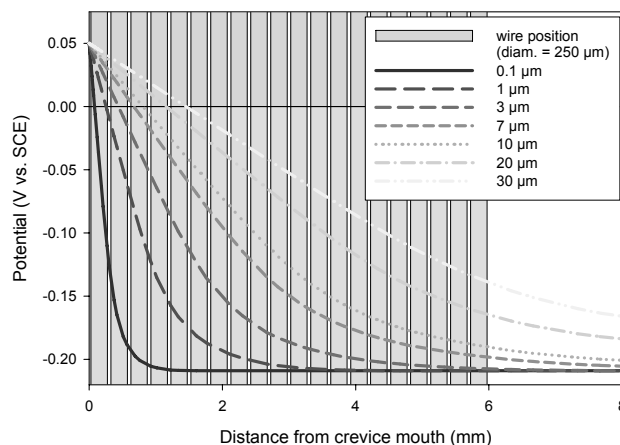
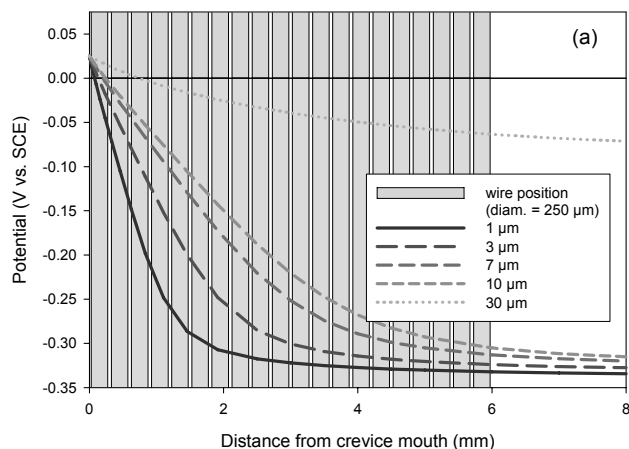


FIGURE 4. Evolution of the potential with distance from the crevice mouth at various crevice gaps for (a) AISI 316 in 1M HCl at ambient temperature for $E_{app}=0.025 V_{SCE}$ and (b) Alloy 625 in 2 M HCl at 60°C for $E_{app}=0.05 V_{SCE}$ (b)

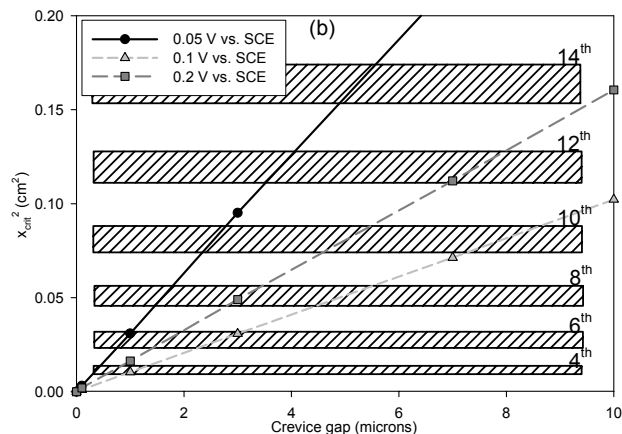
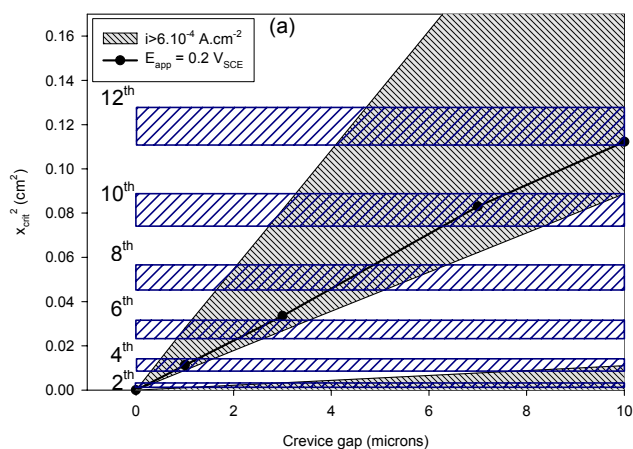


FIGURE 5. x_{crit}^2 vs. crevice gap scaling laws model based on anodic polarization curves for (a) AISI 316 in 1M HCl at ambient temperature and (b) Alloy 625 in 2 M HCl at 60°C. The horizontal lines represent the position of the electrodes of an array (electrode diameter = 0.25 mm) at different distances from the crevice mouth. AISI 316 scaling laws were derived assuming $E_{crit}=-0.2 V_{SCE}$ and $E_H=0.2 V_{SCE}$. The alloy 625 scaling laws were derived assuming $E_{crit}=-0.135 V_{SCE}$.

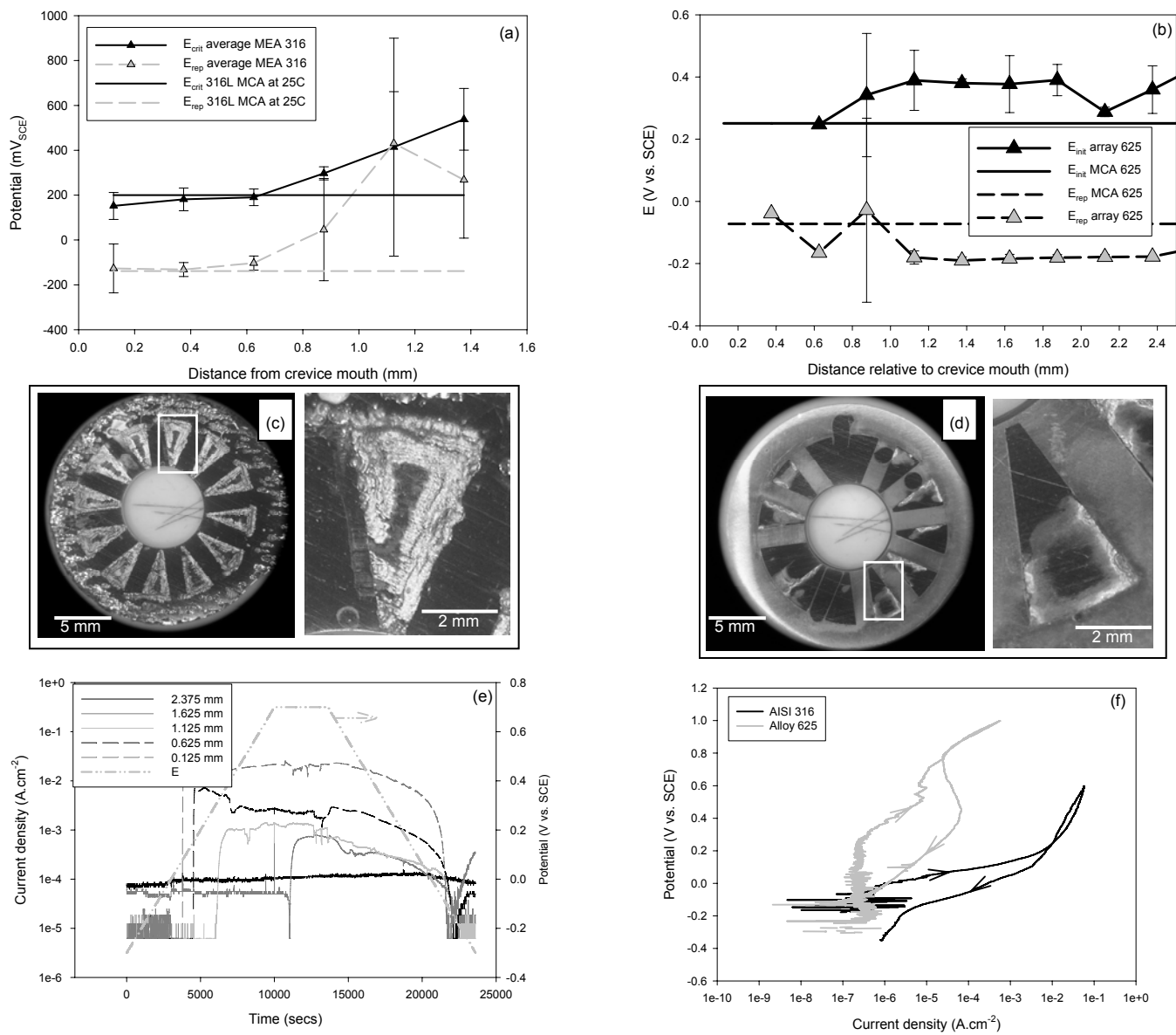


FIGURE 6. Comparison of the critical potentials (E_{crit} and E_{rep}) obtained from (a) AISI 316L stainless steel creviced planar electrode test and AISI 316 stainless steel MEA and (b) alloy 625 MCA and MEA experiments in 0.6 M NaCl at 50°C. (c) optical image of the post-test AISI 316 lollipop sample (reversing potential at $0.6 V_{SCE}$)., One of the plateau teeth marks (circled on the main picture) is enlarged. (d) Optical image of the post-test alloy 625 lollipop sample (reversing potential at $0.6 V_{SCE}$), one of the plateau teeth marks (circled on the main picture) is enlarged. (e) Current density and potential evolution with time for AISI 316 multi electrode array and (f) anodic polarization behavior of AISI 316L and alloy 625 MCA planar electrode, both in 0.6 M NaCl at 50°C.

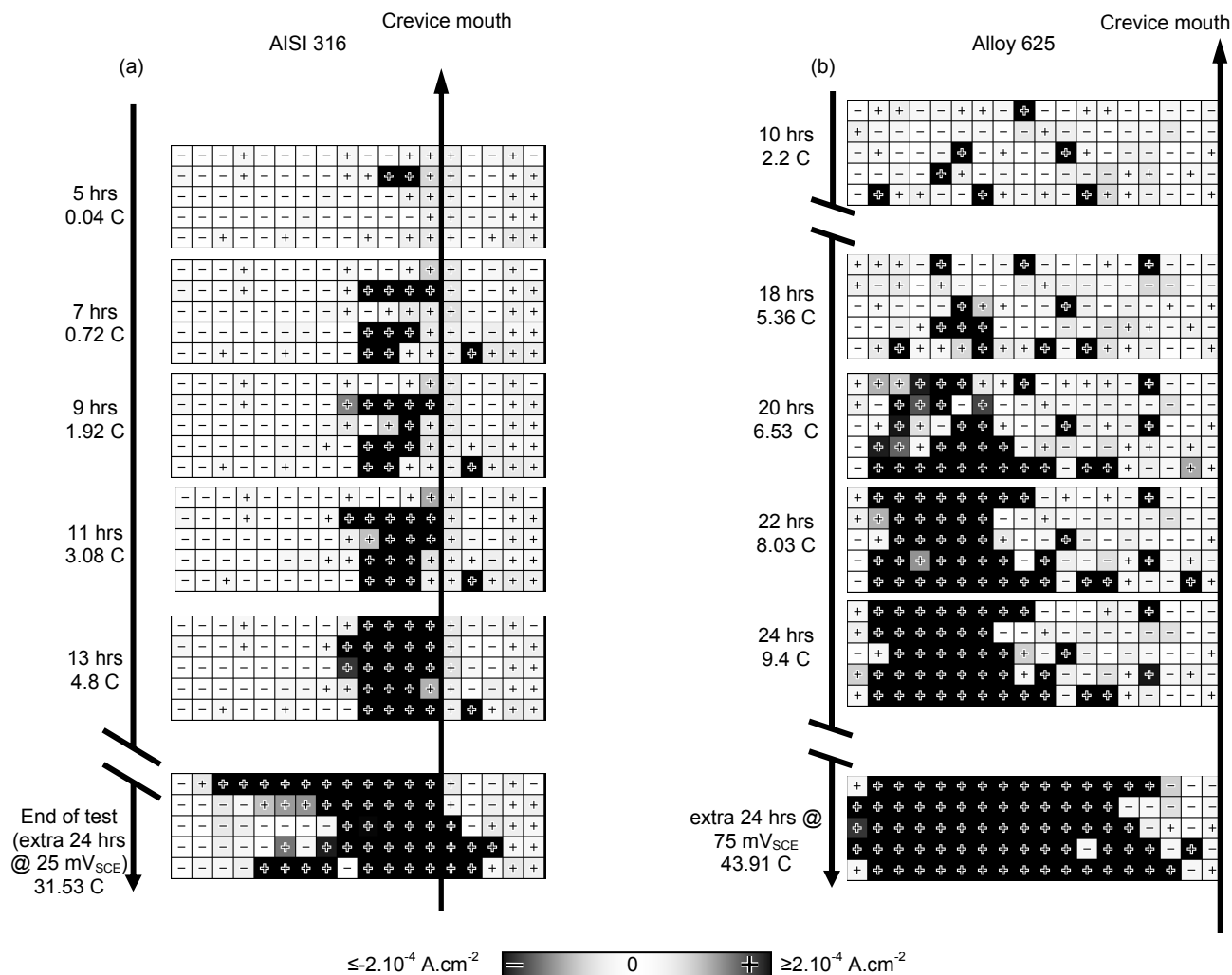


FIGURE 7. Current density map evolution with time of (a) AISI 316 stainless steel and (b) alloy 625 arrays in 0.6 M NaCl at 50°C. Each square represents an electrode with a current density according to the scale. The electrodes covered with the crevice former are left of the arrow. The total charge at each step is given for information. (a) For AISI 316, the current density maps show the initiation and propagation of crevice corrosion during the second step at 0 V_{SCE} . The final map shows the extent of crevice corrosion at the end of the last step at 25 mV_{SCE} . (b) For alloy 625, crevice corrosion only initiate after 18 hours far from the crevice mouth at 50 mV_{SCE} and then propagate closer with time. The final current density map represents the extent of corrosion after an extra 24 hours at 75 mV_{SCE} .

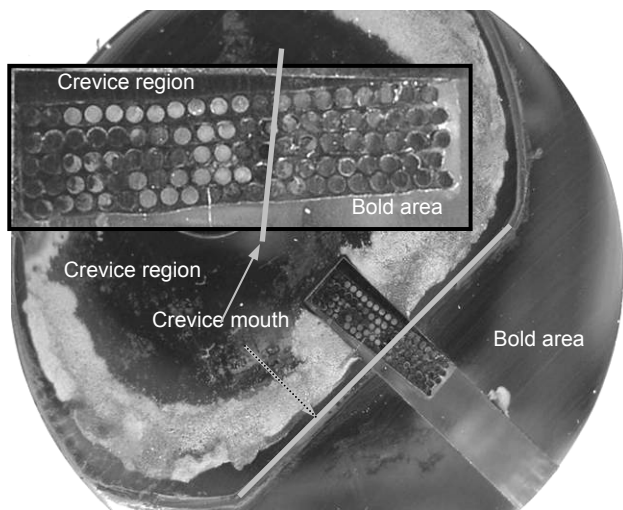


FIGURE 8. Extent of corrosion on the multi-electrode array (insert) and the full setup after 2 days at OCP, 1 day at $-25 \text{ mV}_{\text{SCE}}$, 1 day at 0 V_{SCE} (creviced array) and $-25 \text{ mV}_{\text{SCE}}$ (rest), and 1 day at $25 \text{ mV}_{\text{SCE}}$ (creviced array) and $-25 \text{ mV}_{\text{SCE}}$ (boldly exposed) in 0.6 M NaCl at 50°C with crevice former applied at a torque of 25 inch-lbs.

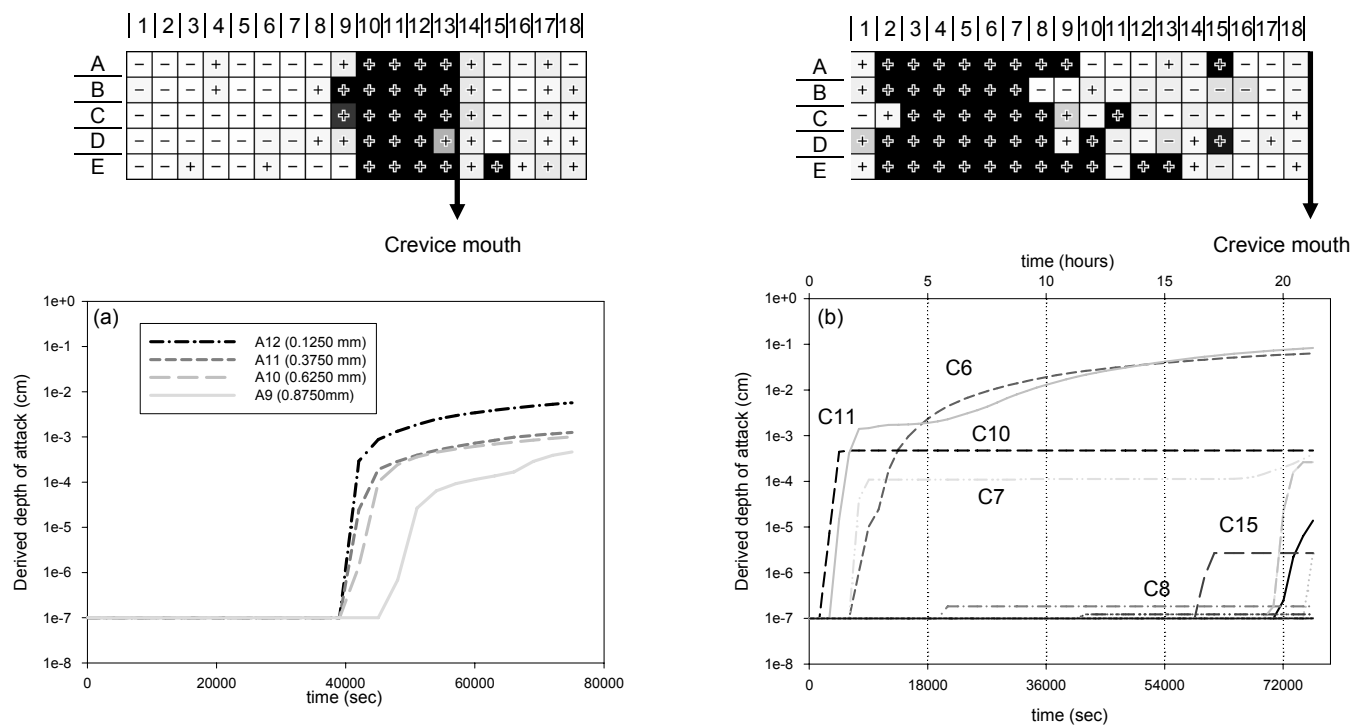


FIGURE 9. Evolution of the derived depth with time of (a) AISI 316 at 0 V_{SCE} and (b) Alloy 625 at $50 \text{ mV}_{\text{SCE}}$ at 50°C at various distances (mm) from the crevice mouth in 0.6 M NaCl . The array notation as well as final current density map is provided for each material along with the position of the crevice mouth. Note that horizontal plateaus are indicators of repassivation.

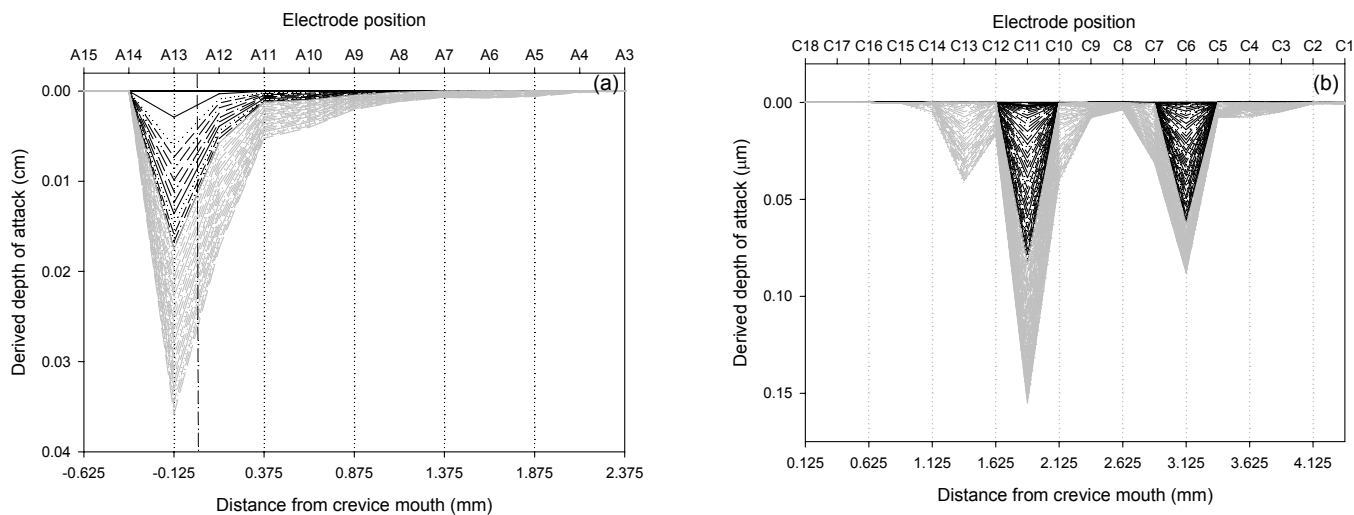


FIGURE 10. Attack depth profiles at 50 minute intervals, derived from the current density for (a) AISI 316 at 0 V_{SCE} (black) and at 25 mV_{SCE} (grey) in 0.6 M NaCl at 50°C and (b) alloy 625 at 50 mV_{SCE} (black) and 75 mV_{SCE} (grey) in 0.6 M NaCl at 50°C. The crevice mouth is at the distance zero (represented by a dash-dot line on (a)).

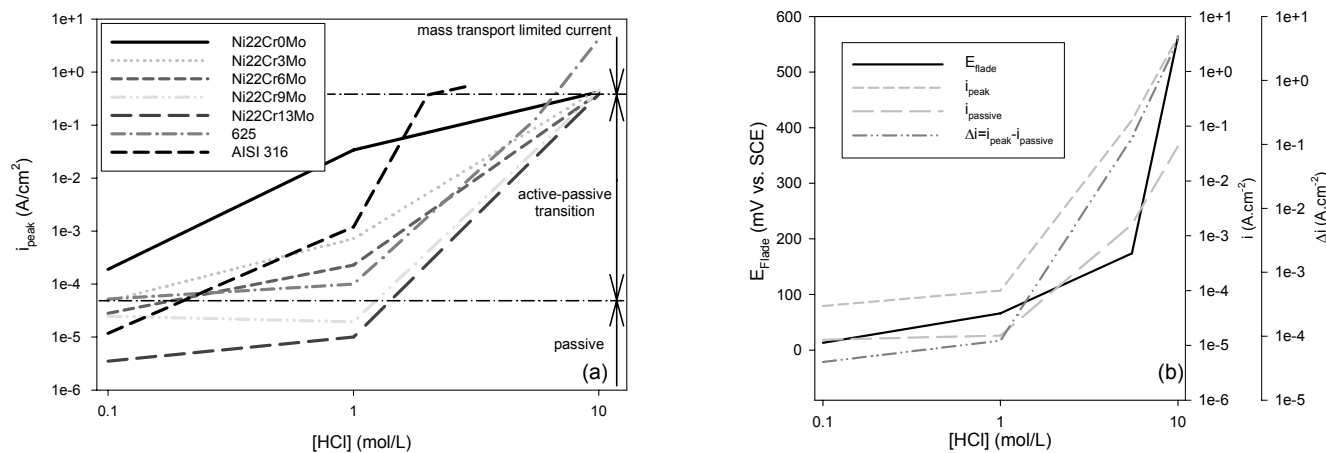


FIGURE 11. (a) Evolution of i_{peak} with HCl concentration at ambient temperature for alloy 625, AISI 316 and various Ni-22Cr-xMo model alloys ($x=0, 3, 6, 9$ and 13 wt%). (b) Evolution of the Flade Potential for alloy 625 in 0.1 M, 1 M and 10 M HCl at ambient temperature as well as i_{peak} , $i_{passive}$ and $\Delta i = i_{peak} - i_{passive}$.